THE JOURNAL OF PHYSICAL CHEMISTRY Letters

Letter

pubs.acs.org/JPCL

Capacitive Dark Currents, Hysteresis, and Electrode Polarization in Lead Halide Perovskite Solar Cells

Osbel Almora,[†] Isaac Zarazua,[†] Elena Mas-Marza,[†] Ivan Mora-Sero,[†] Juan Bisquert,[†,‡] and Germà Garcia-Belmonte*[,†]

[†]Photovoltaic and Optoelectronic Devices Group, Departament de Física, Universitat Jaume I, ES-12071 Castelló, Spain

[‡]Department of Chemistry, Faculty of Science, King Abdulaziz University, Jeddah 21589, Saudi Arabia

Supporting Information

ABSTRACT: Despite spectacular advances in conversion efficiency of perovskite solar cell many aspects of its operating modes are still poorly understood. Capacitance constitutes a key parameter to explore which mechanisms control particular functioning and undesired effects as current hysteresis. Analyzing capacitive responses allows addressing not only the nature of charge distribution in the device but also the kinetics of the charging processes and how they alter the solar cell current. Two main polarization processes are identified. Dielectric properties of the microscopic dipolar units through the orthorhombic-to-tetragonal phase transition account for the measured intermediate frequency capacitance. Electrode polarization caused by interfacial effects, presumably related to kinetically slow ions piled up in the vicinity of the outer interfaces, consistently explain the reported excess capacitance values at low frequencies. In addition, current−voltage curves and capacitive responses of perovskite-based solar cells are connected. The observed hysteretic effect in the dark current originates from the slow capacitive mechanisms.

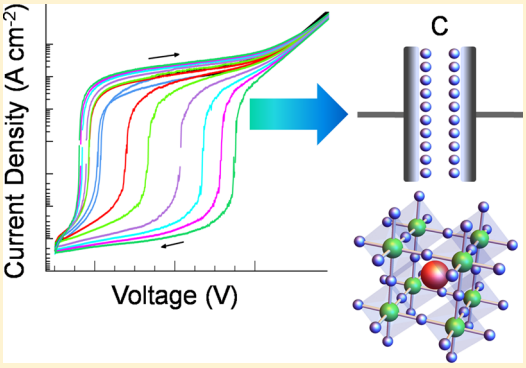

Hybrid lead halide perovskite solar cells have emerged in the last three years,[1] boosting the achieved solar to electricity power conversion efficiency to values as high as 20.1%.[2] Previous expectations signaling 20%-efficiency forecasts[3] have been already exceeded and the current development of the technology points toward and beyond 25%.[4] Variations of cell configuration, selective contacts, and kinds of perovskite utilized have been explored during this short period.[3−5] The most extensively studied structure comprises $CH_3NH_3PbI_3$ ($MAPbI_3$) perovskite (or its analogous but using chlorine precursor: $CH_3NH_3PbI_{3-x}Cl_x$) as absorber materials, in combination with electron-(TiO_2) and 2,2′,7,7′-tetrakis(*N*,*N*-dipmethoxyphenylamine)-9,9-spirobifluorene (*spiro*-OMeTAD) hole-selective contacts. The organic cation $CH_3NH_3^+$ is mainly responsible for the structural stability of the perovskite structure, whereas the electronic properties are largely determined by metal and halide hybridized orbitals.[6−8]

In spite of the spectacular advances in cell efficiency, many aspects of this system are poorly understood. In particular, the interpretation of frequency dependence capacitance in $MAPbI_3$ and related inorganic−organic perovskites remains unsettled at this time. One interesting phenomenon is the giant dielectric constant that is observed at ultraslow frequency, which is amplified under illumination.[9] In addition, there are different mechanisms contributing to the capacitance, which may be chemical or dielectric, including contact and bulk capacitance, and possible ferroelectric effects. These capacitive properties have been investigated in some reports,[10−12] but due to the complex morphology of perovskite solar cells and the combination of ionic−electronic properties, a consistent picture of the capacitances to assist device understanding has not been developed yet. Analyzing capacitive responses allows addressing not only the nature of charge distribution in the device but also the kinetics of the charging processes and how they alter the solar cell current. Therefore, we have checked extensively capacitive mechanisms of $MAPbI_3$ cells that we thoroughly describe in this paper. We first address the hysteresis effect by direct treatment of current density−voltage ($J-V$) curves in the dark and connect it to the cell capacitance. In order to clarify the origin of the different capacitive processes observed, we perform the measurements as a function of temperature and film thickness and provide for the first time a complete interpretation of separate capacitive effects in perovskite solar cells.

An intriguing effect manifested as a hysteretic response of the $J-V$ curves upon illumination has been extensively reported.[6,10,13,14] Hysteresis has a detrimental influence on the photovoltaic operation reliability and stability so as to advance in its alleviation. Although the origin of hysteretic effects is still unclear, there are several mechanisms that have already been proposed. Ferroelectric properties of the perovskite materials appear as an underlying mechanism in some reports,[15−17]

Received: March 6, 2015
Accepted: April 13, 2015
Published: April 13, 2015

DOI: 10.1021/acs.jpclett.5b00480
J. Phys. Chem. Lett. 2015, 6, 1645−1652

whereas other works highlight delayed electronic trapping processes.[18] In addition, slow ion migration might consistently produce hysteretic responses in the current−voltage characteristics.[13,19,20] In order to progress in clarifying the phenomenon, a discerning experimental technique should be adopted. Among other approaches, capacitance may be a key parameter to explore which mechanisms originate hysteretic effects. It is known that upon illumination, perovskite-based solar cells exhibit a giant capacitance observable in the low frequency response.[9] Even in dark conditions, an extra capacitance appears in excess of geometrical or chemical capacitances[21] operating at intermediate or high-frequency parts of the capacitance spectra. A connection between the low-frequency capacitance and the hysteretic effect of the current−voltage curves upon illumination has also been suggested,[10,22] but an experimental correlation is still lacking.

We connect here $J-V$ curves and capacitive responses of $MAPbI_3$-based solar cells comprising both planar and mesoporous TiO_2 electron selective layers. A method is devised to isolate capacitive currents from operating currents within $J-V$ curves. Dark capacitive currents are responsible for the reported hysteresis and can be assimilated to a constant capacitance contribution at low voltages. This approach correlates with the cell capacitance measured directly at low frequencies (<1 Hz), using impedance spectroscopy. Several mechanisms (ferroelectric, unit cell dipolar, trap states, electrode polarization) are checked in relation to an exhaustive evaluation of the capacitance response as a function of frequency, temperature, $MAPbI_3$ layer thickness and solar cell structure. Because the low-frequency capacitance appears to be independent of the absorber layer thickness, it is concluded that electrode polarization, presumably caused by ions piled up in the vicinity of the outer interfaces, consistently explains the reported capacitance values and, consequently, the observed dark current hysteresis.

Dark Current Hysteresis. One way to explore the relationship between low-frequency, excess capacitance, and hysteresis is by measuring $J-V$ characteristics in the dark at different scan rates for both forward and reverse sweep directions. As the excess capacitance appears at low frequencies (<1 Hz), scan rates should be slow enough to achieve steady-state conditions. Dark conditions have been chosen to reduce nonstabilized light or temperature effects during time-consuming experiments. Figure 1a shows $J-V$ curves registered at slow scan rates ranging from 50 down to 1 mV s^{-1} with solar cells containing mesoporous TiO_2. In the voltage range −0.1—0.4 V, the response depends on the scan sweep direction with a shift of the crossing points at which current changes sign. At low voltages, hysteretic effects are apparent, whereas operating currents collapse into a single response in the high voltage range (>0.5 V). In order to highlight hysteretic response, current is represented in logarithmic scale. The overall effect resembles a capacitive square loop as those reported using electrochemical cyclic voltammetry methods.[23,24] Interestingly, the hysteretic behavior almost disappears for extremely slow scan rates (1 mV s^{-1}), and current attains equilibrium values J_0 (the crossing point approaches voltages near zero). In the studied low-voltage range, J_0 appears to be related to shunt effects and leakage currents. Excess current contributions can be easily determined by comparing the $J-V$ curves at varying scan rates with the equilibrium current as $J_{cap} = J - J_0$. These differences are plotted in Figure 1b, where the expected J_0 is taken from the slowest swept $J-V$ curve as the mean between the two sweep

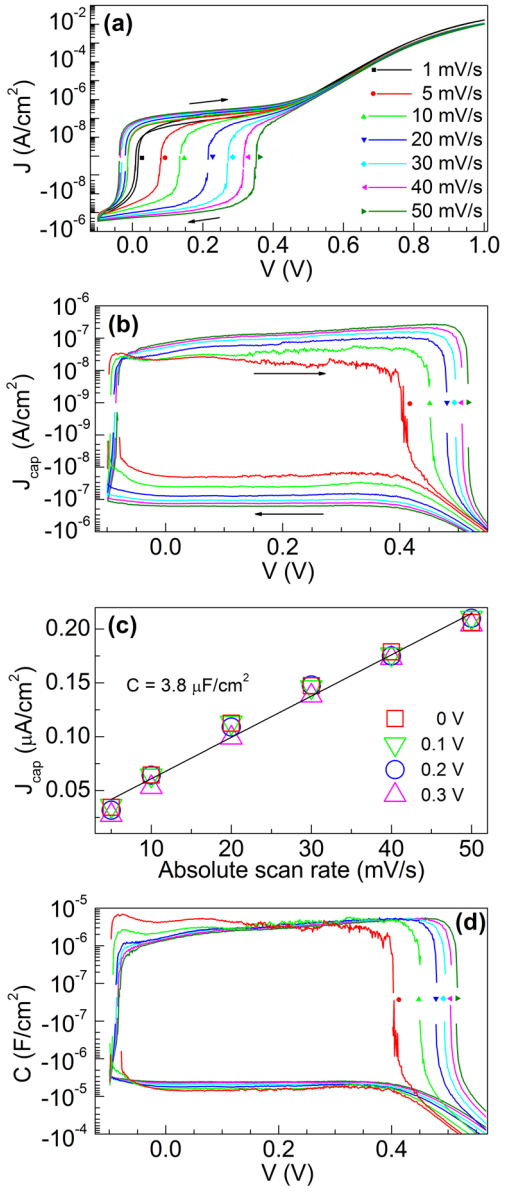

Figure 1. (a) $J-V$ curves at different scan rates as indicated with logarithmic scaled currents. (b) J_{cap} extracted from $J-V$ curves. (c) Current proportional to the scan rate at different applied voltages. (d) Capacitance calculated from J_{cap} s^{-1} at different scan rates as in (a).

senses. J_{cap} can be certainly labeled as capacitive current as deduced from its linear dependence with the scan rate s for different voltages. This is plotted in Figure 1c displaying a linear behavior whose slope corresponds to the capacitance of 3.8 μF cm^{-2}. This correlation derives from the assumption of a voltage-independent capacitance as $J_{cap} = dQ/dt = C\ dV/dt = Cs$.[10] The result of evaluating the previous expression for the curves of Figure 1b is displayed in Figure 1d. One can observe that curves nearly collapse into a square, textbook capacitive case,[25] exhibiting a rather constant capacitance value of ∼3 μF cm^{-2}. Our experiments inform on the presence of capacitive currents in the low-voltage range and how they yield hysteretic-like responses in the $J-V$ curves. Although the experiments are restricted to dark conditions, one would expect even larger effects in the case of illumination when a huge increase in the low-frequency capacitance occurs.[9] Also of interest is the fact that capacitance currents need of extremely slow scan rates to

DOI: 10.1021/acs.jpclett.5b00480
J. Phys. Chem. Lett. 2015, 6, 1645−1652

be eliminated pointing to a retarded kinetics for the mechanisms originating them. Strictly speaking then, one cannot consider the previously reported dark effect as true "hysteresis" due to the fact that it is not permanent upon approaching steady-state conditions.[26]

Capacitance Spectra and Dipolar Polarization. To further understand kinetic effects, one can test solar cell response by varying temperature. To this end, we measure capacitive spectra of perovskite-based solar cells containing mesoporous TiO_2 at different temperatures in the range between 123 to 303 K. Spectra are registered at zero bias, both during cooling and heating, to check response stability as observed in Figure S1 (Supporting Information). A general picture of the measured capacitance spectra is drawn in Figure 2a. The capacitance drop at 1 MHz corresponds to the effect of the series resistance caused by conductive contact layers. Depending on the measuring temperature, different portions of the whole spectrum are visible. Two capacitive steps are identified, which indicates the existence of two distinctive mechanisms. For low-temperature (123 K) spectra, a capacitive plateau is observed in the range of 0.1 μF cm^{-2} that can be assimilated to the high-frequency limit C_∞ (see Figure 2b). Toward low frequencies, a temperature-activated process appears situating the capacitance at a plateau near 1 μF cm^{-2} at much higher temperatures (213 K). By plotting the capacitance measured at 1 kHz as a function of the temperature (Figure 2d), one can observe a rather sharp step at ∼160 K, followed by a slight decrease at higher temperatures. In accordance with previous dielectric measurements,[27] this increment in the capacitance correlates with the phase transitions undergone by perovskite-type materials where the super cell symmetry increases upon heating.[28] At 160 K, $CH_3NH_3PbI_3$ orthorhombic structure (γ-phase) changes to tetragonal structure (β-phase). The capacitance increment measured at 1 kHz in Figure 2c exhibited by $CH_3NH_3PbI_{3-x}Cl_x$-based cells can be then interpreted accordingly. The phase transition kinetics is characterized by an activation energy calculated from the dependence of the inflection point of the capacitance step on temperature. Alternatively, the activation energy can be calculated from the temperature shift in the capacitance derivative peak as observed in Figure S2 (Supporting Information). The activation energy for the orthorhombic-tetragonal transition is determined to be approximately equal to 0.25 eV as observed in Figure S3 (Supporting Information). It is interpreted as a potential barrier for the neighboring transitions of the polarizable units. Recently, polarization in the tetragonal phase has been explained in terms of rotations of $CH_3NH_3^+$ cation dipoles.[29] As known, $CH_3NH_3^+$ does not occupied a fixed position in the structure (dynamic disorder) thus contributing to the increase in polarizability.[30] However, other polarization mechanisms are also feasible. PbI_6 octahedra making up the external perovskite structure rotate around the c axis.[31,32] Moreover cooperative ionic off-centering might contribute to local polarization, eventually giving rise to long-range ion displacement and macroscopic polarization.[13] Regarding local dipolar units, a simple calculation based on the Kirkwood–Fröhlich equation[33]

$$\frac{(\varepsilon - \varepsilon_\infty)(2\varepsilon + \varepsilon_\infty)\varepsilon_0}{\varepsilon(\varepsilon_\infty + 2)^2} = \frac{N\mu^2}{9k_BT} \quad (1)$$

allows relating the measured relative permittivity values corresponding to the intermediate temperature capacitance plateau ($\varepsilon \approx 192$ in Figure 2c) to the dipole moment μ of the polarizing units. In eq 1, N is the volume density of dipoles, k_B the Boltzmann constant, and T the absolute temperature. ε_∞ accounts for the high-frequency relative permittivity limit, and ε_0 corresponds to the vacuum permittivity. Equation 1 is in fact an approximation that assumes noninteracting dipoles. We note that the relative permittivity 192 resulting from the capacitance values constitutes an overestimation that does not consider the roughness effect produced by the mesoporous matrix.[11] More reasonable permittivity values in the reported range of 24–36

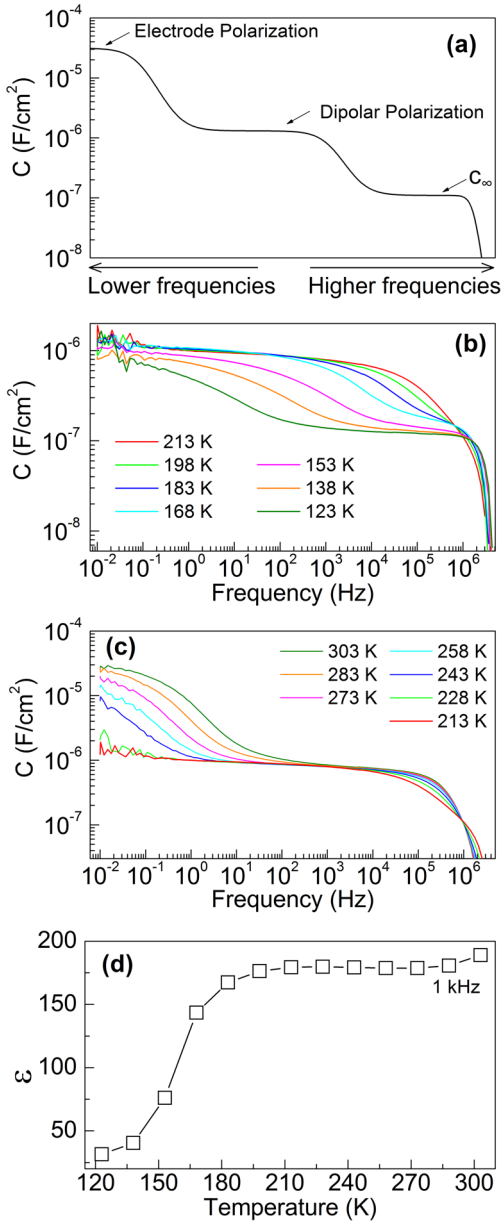

Figure 2. (a) General view of the capacitance spectra in dark at zero bias showing the main mechanisms responsible for capacitive steps: at higher-frequencies (lower temperatures) a step occurs by the permittivity increase related to the dipolar polarization in the orthorhombic-to-tetragonal phase transition. At lower frequencies (higher temperatures), the capacitance step is caused by electrode polarization. Capacitance spectra at different temperatures in the ranges (b) 123–213 K and (c) 213–303 K. (d) Relative permittivity as a function of temperature measured at 1 kHz without considering the roughness effect.

DOI: 10.1021/acs.jpclett.5b00480
J. Phys. Chem. Lett. 2015, 6, 1645–1652

give rise to roughness factors ~6,[15,34](see later measurements with planar TiO_2 structures). Regarding the roughness effect, a dipole moment of order $\mu \approx 7.1 \times 10^{-30}$ C m (2.1 D) can be estimated, assuming $N = 3.95 \times 10^{21}$ cm^{-3},[27] which can be related to diverse dipolar mechanisms ($CH_3NH_3^+$ or PbI_6 octahedra reorientation, and cooperative ionic off-centering) previously commented upon. The high capacitance plateau in Figure 2b, related to the phase transition, is observed at lower frequencies even at temperatures as low as 120 K. This is because the capacitance step occurs at higher frequencies when the temperature is raised up as expected for an activated process. We point out that the dipolar interpretation of this capacitance is consistent with the absorber layer thickness test as later explained.

At higher temperatures, $CH_3NH_3PbI_3$ exhibits another phase transition in which tetragonal phase evolves to a cubic structure (α-phase).[28] This tetragonal-to-cubic transition has been determined to occur at ~330 K. As already stated, X-ray diffraction patterns show the gradual disappearance of the 211 reflection associated with the tetragonal supercell as the temperature increases.[35] The transition is not sharp but gradual within a temperature interval of 50 K. By examining Figure 2c, one can observe the progressive appearance of a low-frequency capacitance in excess of the geometrical value reached with the tetragonal phases at intermediate temperatures. At approximately 10 mHz, the capacitance step toward low frequencies is nearly completed attaining values of 30 μF cm^{-2} at 300 K. The high-temperature process also follows an activated mechanism with activation energy equal to 0.45 eV as observed in Figure S3 (Supporting Information). A similar calculation than that performed for the tetragonal phase using eq 1 results in similar dipole moment order $\mu \approx 12 \times 10^{-30}$ C m (3.5 D). Again the dipole moments encountered results in reasonable values being the measured large permittivity an effect of the local field correction as described in eq 1. However the interpretation of the low-frequency capacitance in terms of a dipolar mechanism fails at checking the response upon $MAPbI_3$ thickness variation.

We note here that the capacitance value extracted from the $J-V$ curve analysis of the capacitive currents in Figure 1 corresponds to capacitive values obtained at room-temperature in the 1 Hz frequency range. The capacitive value extracted by the current method (3.8 μF cm^{-2}) lies below the low-frequency capacitance spectra plateau of Figure 2c of 30 μF cm^{-2}, presumably because both procedures are not strictly comparable. The capacitive current is derived from large-amplitude sweep of applied bias voltage, whereas capacitance spectra result from small-amplitude perturbation over steady-state zero bias. It is then not surprising that larger capacitances are extracted by small-amplitude methods because even for sweep speeds as slow as 1 mV s^{-1}, the current response has not attained steady-state conditions. Nevertheless, we can certainly infer that the hysteretic effect observed in the dark has a capacitive origin in the low-frequency excess capacitance. The slow kinetics of the excess capacitance explains the extremely low scan rate needed for hysteresis suppression.

The previous experiments point to the fact that the capacitive response of $CH_3NH_3PbI_{3-x}Cl_x$-based solar cells can be consistently interpreted in terms of the dielectric properties of the absorber material. The capacitance singularity around 160 K clearly correlates with the increment of the supercell symmetry undergoing the $\beta-\gamma$ phase transition. However the high-temperature capacitance step cannot be linked with the subsequent increase in the structure symmetry that occurs around 330 K (α-phase) as later explained. It should be noted here that any attempt to observe ferroelectric effects in addition to the capacitive responses previously discussed has been unsuccessful. As explained in Figure S4 (Supporting Information), the use of the Sawyer–Tower circuit, even at low enough frequencies that the excess capacitance is observed, does not yield any evidence of remnant polarization.

Thickness Dependence and Electrode Polarization. A suitable test, aimed at discerning whether purely dielectric mechanisms originate the capacitances found in Figure 2, consists of investigating how capacitance scales with the perovskite layer thickness. For this purpose, planar perovskite solar cells with structure FTO/TiO_2(compact)/$MAPbI_3$/*spiro*-OMeTAD/Au were prepared varying the $MAPbI_3$ layer thickness L between 400 and 200 nm. Planar solar cells reproduce the general trends of the capacitance spectra measured for devices comprising mesoporous TiO_2 of Figure 2 as observed in Figure S5 (Supporting Information). In this case, it is easier to calculate the $MAPbI_3$ layer thickness because of the sandwiched structure. By examining Figure 3, one can observe that at

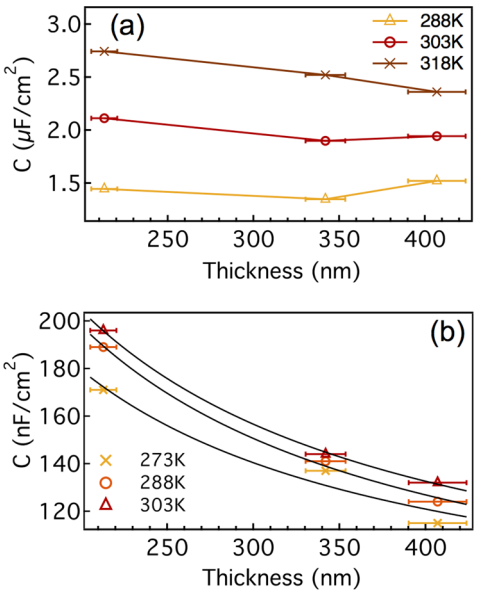

Figure 3. Capacitance as a function of the perovskite layer thickness at different temperatures extracted from (a) a low-frequency plateau corresponding to the electrode polarization and (b) an intermediate frequency plateau caused by dipolar polarization.

low-temperature the intermediate-frequency capacitance plateau of Figure 2b, which corresponds to the capacitive value reached after the $CH_3NH_3PbI_3$ orthorhombic to tetragonal phase transition is completed, scales with the inverse of the layer thickness. Lines in Figure 3b state for fittings using the expression $C = (\varepsilon\varepsilon_0/L) + C_0$, in which the adding term C_0 might account for the capacitive effect of the contacting layers and the high frequency contribution C_∞ of the $MAPbI_3$ film.[36] From the fitting at room temperature, it is obtained that $\varepsilon = 32.5 \pm 0.7$, being in good consistency with reported values.[15,34] It is worth remarking here that the analyzed samples comprise multilayer structures that can be modeled as a first approach by the series connection of parallel RC subcircuits corresponding to each individual layer. The perovskite capacitance dominates the response at intermediate and low frequencies in those cases in which contacting layers (*spiro*-OMeTAD and TiO_2) possess

DOI: 10.1021/acs.jpclett.5b00480
J. Phys. Chem. Lett. 2015, 6, 1645–1652

high enough conductivity so as to displace their response to the high-frequency part of the spectra.

One can then infer a purely dielectric origin for the capacitive step occurring at 160 K in Figure 2d and relate it to the $MAPbI_3$ film. It is also noted that capacitance slightly decreases with temperature. When the thickness test is performed on the low-frequency, high-temperature capacitive step, a completely different dependence is extracted. As observed in Figure 3a, capacitance results are practically independent of the $MAPbI_3$ film thickness. This last finding would entail that polarization mechanisms underlying the low-frequency dark capacitance cannot be easily assimilated to purely dielectric bulk phenomena. In the next, alternative explanations will be confronted with the experimental observation of a thickness-independent low-frequency excess capacitance.

Excess capacitance has been recently related to the occupancy of electronic traps within the $MAPbI_3$ film following a given density-of-states (DOS) $g(E)$.[18,37,38] The slow trap kinetics would explain the low-frequency capacitive response and the consequent hysteretic $J-V$ curve. Electronic DOS can be easily determined from the capacitance spectra derivative according to[39]

$$g(E) = -\frac{V_{bi}}{qLk_BT}\frac{dC(\omega)}{d(\ln \omega)} \quad (2)$$

Here, ω accounts for the angular frequency, and V_{bi} is the built-in voltage produced by the workfunction offset. Full depletion conditions should be accomplished to have the absorber layer thickness L in eq 2 instead of the depletion layer width. As was recently discussed for planar perovskite solar cells, full depletion surely occurs at zero-bias because of large V_{bi} and relatively low doping levels.[36] Equation 2 has been largely used in inorganic solar cells,[39] and it was introduced by us in the field of organic photovoltaics.[40] Measuring frequency ω modulates the so-called demarcation energy[41] $E = k_BT\ln(\omega_0/\omega)$ that explores the bandgap DOS cumulatively contributing to the capacitance. ω_0 denotes the response frequency that states the time scale of the capture-release electronic process. By integration in eq 2 over frequency (energy), one readily infers that the excess capacitance ΔC is proportional to the layer thickness as

$$\Delta C = \frac{qL}{V_{bi}}\int g(E)dE \quad (3)$$

Therefore, interpretation of the low-frequency capacitance step in terms of the occupancy of bulk electronic DOS would entail $\Delta C \propto L$ as for purely chemical capacitance, clearly in contradiction with our observation in Figure 3a. Thickness-independent capacitance might be still consistent with this approach in the particular case that electronic DOS is restricted to a portion of whole $MAPbI_3$ layer, although the reported slow kinetics is hardly explained by means of purely electronic transitions.

The independence of the excess capacitance with the layer thickness suggests an origin related to interfacial mechanisms. Trapping of electronic carriers or ionic charges might accumulate at the contact interface altering the local electrical field. As a consequence, thin space charge regions can be formed in the vicinity of the contacts, an effect known as electrode polarization for ionic conductors.[42,43] In these cases, the excess capacitance relates to the width of the space charge region w instead of the layer thickness as $\Delta C = \varepsilon\varepsilon_0/w$.[44] Accordingly, excess capacitance has a purely electrostatic origin, although contributions arising from molecular absorption or electrode reaction might also take place.[44,45] This last relationship yields values $w \approx 5.7$ nm from our measurements at room temperature of cells containing mesoporous TiO_2, and $w \approx 13$ nm for oxide planar layers. From this approach, properties of the interface rather than bulk mechanisms explain the excess capacitance being consistent with the layer-thickness independence because $w \ll L$. For purely ionic conductors, we proposed the interpretation of the excess capacitance as originated by mobile ions piled up near the metallic contacts.[46] At low enough frequencies, mobile ions accumulate near one of the outer interfaces and are removed from the opposite interface depending on the electrical field direction. As occurring in ionic conductors electrode polarization may explain the observed excess capacitance as originated by ion accumulation (or depletion) zones in the $MAPbI_3$ bulk attaching the electrode interfaces. This mechanism would be in accordance with recent proposals that link mobile ions to the explanation of hysteretic features.[13,26] Assuming ion continuity and Poisson electrostatic relations, the interfacial space charge at zero volts is confined within the ionic Debye length L_D as

$$L_D = \sqrt{\frac{\varepsilon\varepsilon_0 k_BT}{q^2 n}} \quad (4)$$

Here, n states for the density of mobile ions forming the interfacial space charge. The space charge capacitance is derived by equaling the ionic Debye length to the space charge width giving the following expression

$$C_{sc} = \frac{\varepsilon\varepsilon_0}{L_D} \quad (5)$$

We note that eq 5 results from equilibrium conditions, not valid when bias voltage is applied. Previous frequency-dependent capacitance calculations agree with eq 5 in the low-frequency limit.[47] Equation 5 corresponds to the excess capacitance generated by one interface. When the two outer contacts intervene, the calculation must consider the series connection of two capacitors. A simple calculation using eq 5 at room temperature yields space charge density values of 2.4×10^{17} cm^{-3} for planar cells and greater values for mesoporous devices ($n = 1.4 \times 10^{18}$ cm^{-3}) presumably because of the larger interface area. Assuming that the mobile ionic charge is formed by the iodine anions or ionic defects, these last calculations imply an excess of ions around 0.01% that accumulate at the interface. The potential drop caused by the space charge can be easily determined from $\Delta V = qnw/C_{sc}$. It results in approximately 25 mV for both types of solar cells, in good agreement with the assumption in eq 4 that thermal energy originates charge accumulation with Debye length extension. Space charge layers only produce then a slight screening of the electrical field originated by the built-in voltage. Hence, the screening effect of piled-up ions is not able to significantly lower the expected $V_{bi} \approx 1.2$ V (mainly caused by the workfunction offset between $MAPbI_3$ and TiO_2)[36] in accordance with the large flat-band voltage (~1.0 V) extracted from Mott–Schottky analyses and the voltage profile determined by Kelvin probe measurements.[36] Within this approach, the slow kinetics is related to the ionic dynamics of interfacial pile-up.[47] The thermally activated process of Figure 2c appears as a consequence of the increased ion conductivity as the temperature is raised up.

DOI: 10.1021/acs.jpclett.5b00480
J. Phys. Chem. Lett. 2015, 6, 1645–1652

The previous experiments have revealed that hysteretic-like loops in the $J-V$ curves observed in dark conditions around room temperature are related to the excess capacitance in the low-frequency part. This capacitive increase might be consistent with a bulk dipolar mechanism occurring inside the unit cell in the onset of the tetragonal to cubic phase transition. However, the thickness-independent capacitive values at low frequencies allow ruling out purely dielectric explanations as, in this last case, capacitance would depend inversely on the absorber layer thickness. Other electronic mechanisms that scale with L as occurred with the chemical capacitance can also be discarded. The electrode polarization explanation proposed here is consistent with the thickness test as it restricts their effect to the space charge region width. In this approach, interface properties control the capacitive increase in the low-frequency part of the spectra. We stress here that the derivation of eq 5 only assumes electrostatic interactions and discards electrode reactivity effects. When strong interactions between contacting materials and $MAPbI_3$ occur, the capacitance should incorporate both electronic and ionic contributions in a much more complex way.

We note here that our experiments have only addressed dark properties. These findings indeed constitute a necessary starting point to progress into the rich and varied scenario that appears upon light irradiation of perovskite-like photovoltaic materials. As already mentioned, illumination induces giant capacitive responses at low frequencies,[9] likely signaling light-driven structural changes abled to promote local polarization[48] and ion rearrangement.[49] In a recent study, it has been observed that light induces highly reversible sub-bandgap absorption peaks and segregation into two crystalline phases.[50] In addition, light soaking, particularly for solar irradiation levels, increases the temperature of the absorber layer. Recalling that the $MAPbI_3$ cubic phase transition undergoes around 330 K, a complex interplay appears, in which electronic, structural, and ionic properties might get strongly entangled.

In summary, we have checked several mechanisms (ferroelectric, dipolar polarization, trap states, electrode polarization) for consistency in relation to an exhaustive evaluation of the capacitance response of $MAPbI_3$ solar cells. Capacitance has been recorded as a function of frequency, temperature, $MAPbI_3$ layer thickness, and solar cell structure. Two main polarization mechanisms are identified in dark conditions: (i) dipolar units giving rise to dielectric response through the orthorhombic-to-tetragonal phase transition, and (ii) electrode polarization caused by outer contact charging, presumably originated by ion interfacial accumulation. This last mechanism allows explaining the perovskite layer's excess capacitance, which consequently causes the observed current hysteresis.

EXPERIMENTAL METHODS

In this study, $CH_3NH_3PbI_{3-x}Cl_x$ perovskite is used in a structure with and without mesoporous scaffold of the type: FTO/TiO_2(compact)/TiO_2(mesoporous)/$MAPbI_3$/*spiro*-OMeTAD/Au and FTO/TiO_2(compact)/$MAPbI_3$/*spiro*-OMeTAD/Au, respectively. All the studied cells were prepared over FTO glasses (25 × 25 mm, Pilkington TEC15, ∼15 Ω/sq resistance), which were partially etched with zinc powder and HCl (2 M) in order to avoid short circuits, obtaining 0.25 cm^2 of active electrode area. The substrates were cleaned with soap (Hellmanex) and rinsed with Milli-Q water and ethanol. Then, the sheets were sonicated for 15 min in a solution of acetone:isopropanol (1:1 v/v), rinsed with ethanol, and dried with compressed air. After that, the substrates were treated in a UV−O_3 chamber for 20 min. The TiO_2 blocking layer was deposited onto the substrates by spray pyrolysis at 480 °C, using a titanium diisopropoxidebis(acetylacetonate) (75% in isopropanol, Sigma-Aldrich) solution diluted in ethanol (1:39, v/v), with oxygen as carrier gas. The spray was performed in 4 steps of 12 s, spraying each time 10 mL (approx.), and waiting 1 min between steps. After the spraying process, the films were kept at 480 °C for 5 min. Subsequently, a UV−O_3 treatment was performed for 20 min. When needed, for cells with mesoporous scaffold, the mesoporous TiO_2 layer was deposited by spin coating at 4000 rpm during 60 s using a TiO_2 paste (Dyesol 18NRT, 20 nm average particle size) diluted in terpineol (1:3, weight ratio). After drying at 90 °C for 10 min, the TiO_2 mesoporous layer was heated at 470 °C for 30 min and later cooled to room temperature. The thickness determined by scanning electron microscopy was of approximately 200 nm observed in Figure S6 (Supporting Information). The perovskite precursor solution was prepared by reacting 2.64 mmol of CH_3NH_3I and 0.88 mmol of $PbCl_2$ (3:1 molar ratio) in 1 mL of DMF. For the cells with mesoporous scaffold, 100 μL of this solution was spin-coated inside a glovebox, at 2000 rpm for 60 s. For the case of the planar configuration (cells without scaffold), spin-coating speeds were 1000, 2000, and 4000 rpm for perovskite thickness ∼210, 340, and 420 nm, respectively, as observed in Figure S7 (Supporting Information). After the deposition, the substrate was kept at 100 °C for 10 min. Next, the substrates were heated at 100 °C during 90 min in an oven under air stream. Then, the perovskite films were covered with the hole-transporting material (HTM, ∼300 nm thick) by spin coating at 4000 rpm for 30 s under air conditions, using 100 μL of spiro-OMeTAD solution. The spiro-OMeTAD solution was prepared by dissolving in 1 mL of chlorobenzene 72.3 mg of (2,2′,7,7′-tetrakis(*N*,*N*′-di-*p*-methoxyphenylamine)-9,9′-spirobifluorene), 28.8 μL of 4-*tert*-butylpyridine, and 17.5 μL of a stock solution of 520 mg/mL of lithium bis(trifluoromethylsulfonyl)imide in acetonitrile. Finally, 60 nm of gold was thermally evaporated on top of the device to form the electrode contacts using a commercial Univex 250 chamber, from Oerlikon Leybold Vacuum. Before beginning the evaporation, the chamber was evacuated until pressure of 2×10^{-6} mbar. The active electrode area of 0.25 cm^2 per pixel is defined by the FTO and the Au contacts.

Current density−voltage $J-V$ curves were recorded under AM 1.5 100 mW/cm^{-2} simulated sunlight (ABET Technologies Sun 2000) previously calibrated with an NREL-calibrated Si solar cell. The obtained efficiencies using a 0.11 cm^2 mask were about 10% as observed in Table S1 and Figure S8 (Supporting Information). The dark $J-V$ curves were measured with a PGSTAT-30 from Autolab using different scan rates. For the measurement of capacitance spectra as a function of the temperature, an Alpha-N analyzer was employed with a Quatro Cryosystem temperature controller from Novocontrol Technologies. The AC voltage perturbation was of 10 mV and a constant zero bias was kept. Each frequency spectrum was measured ranging between 0.01 Hz and 13 MHz at a given constant temperature, which was changed between 303 and 123 K with steps of 15 K.

DOI: 10.1021/acs.jpclett.5b00480
J. Phys. Chem. Lett. 2015, 6, 1645−1652

■ ASSOCIATED CONTENT

Supporting Information

Experimental results on $J-V$ curves, capacitance spectra, activation energy calculation of the polarizing mechanisms, ferroelectric measurement circuit details, and solar cells SEM images. This material is available free of charge via the Internet at http://pubs.acs.org.

■ AUTHOR INFORMATION

Corresponding Author

*E-mail: garciag@uji.es. Tel.: +34 964 387538.

Notes

The authors declare no competing financial interest.

■ ACKNOWLEDGMENTS

We thank financial support by MINECO of Spain (project MAT2013-47192-C3-1-R), and Generalitat Valenciana (project ISIC/2012/008 Institute of Nanotechnologies for Clean Energies). E.M.-M. thanks the Ramón y Cajal program, and I. Z. thanks CONACYT for a postdoctoral fellow. SCIC services at UJI are also acknowledged.

■ REFERENCES

(1) Green, M. A.; Emery, K.; Hishikawa, Y.; Warta, W.; Dunlop, E. D. Solar Cell Efficiency Tables (Version 42). *Prog. Photovoltaics: Res. Appl.* **2013**, *21*, 827−837.

(2) Green, M. A.; Emery, K.; Hishikawa, Y.; Warta, W.; Dunlop, E. D. Solar Cell Efficiency Tables (Version 45). *Prog. Photovoltaics: Res. Appl.* **2015**, *23*, 1−9.

(3) Park, N.-G. Organometal Perovskite Light Absorbers Toward a 20% Efficiency Low-Cost Solid-State Mesoscopic Solar Cell. *J. Phys. Chem. Lett.* **2013**, *4*, 2423−2429.

(4) Snaith, H. J. Perovskites: The Emergence of a New Era for Low-Cost, High-Efficiency Solar Cells. *J. Phys. Chem. Lett.* **2013**, *4*, 3623−3630.

(5) Burschka, J.; Pellet, N.; Moon, S.-J.; Humphry-Baker, R.; Gao, P.; Nazeeruddin, M. K.; Grätzel, M. Sequential Deposition as a Route to High-Performance Perovskite-Sensitized Solar Cells. *Nature* **2013**, *499*, 316−319.

(6) Snaith, H. J.; Abate, A.; Ball, J. M.; Eperon, G. E.; Leijtens, T.; Kimberly, N.; Stranks, S. D.; Wang, J. T.-W.; Wojciechowski, K.; Zhang, W.; Noel, N. K. Anomalous Hysteresis in Perovskite Solar Cells. *J. Phys. Chem. Lett.* **2014**, *5*, 1511−1515.

(7) Yin, W.-J.; Shi, T.; Yan, Y. Unusual Defect Physics in $CH_3NH_3PbI_3$ Perovskite Solar Cell Absorber. *Appl. Phys. Lett.* **2014**, *104*, 063903.

(8) Even, J.; Pedesseau, L.; Jancu, J.-M.; Katan, C. Importance of Spin−Orbit Coupling in Hybrid Organic/Inorganic Perovskites for Photovoltaic Applications. *J. Phys. Chem. Lett.* **2013**, *4*, 2999−3005.

(9) Juárez-Pérez, E. J.; Sánchez, R. S.; Badia, L.; Garcia-Belmonte, G.; Kang, Y. S.; Mora-Sero, I.; Bisquert, J. Photoinduced Giant Dielectric Constant in Lead Halide Perovskite Solar Cells. *J. Phys. Chem. Lett.* **2014**, *5*, 2390−2394.

(10) Sanchez, R. S.; Gonzalez-Pedro, V.; Lee, J.-W.; Park, N.-G.; Kang, Y. S.; Mora-Sero, I.; Bisquert, J. Slow Dynamic Processes in Lead Halide Perovskite Solar Cells. Characteristic Times and Hysteresis. *J. Phys. Chem. Lett.* **2014**, *5*, 2357−2363.

(11) Pockett, A.; Eperon, G. E.; Peltola, T.; Snaith, H. J.; Walker, A.; Peter, L. M.; Cameron, P. J. Characterization of Planar Lead Halide Perovskite Solar Cells by Impedance Spectroscopy, Open-Circuit Photovoltage Decay, and Intensity-Modulated Photovoltage/Photocurrent Spectroscopy. *J. Phys. Chem. C* **2015**, *119*, 3456−3465.

(12) Pascoe, A. R.; Duffy, N. W.; Scully, A. D.; Huang, F.; Cheng, Y.-B. Insights into Planar $CH_3NH_3PbI_3$ Perovskite Solar Cells Using Impedance Spectroscopy. *J. Phys. Chem. C* **2015**, *119*, 4444−4453.

(13) Unger, E. L.; Hoke, E. T.; Bailie, C. D.; Nguyen, W. H.; Bowring, A. R.; Heumüller, T.; Christoforod, M. G.; McGehee, M. D. Hysteresis and Transient Behavior in Current−Voltage Measurements of Hybrid-Perovskite Absorber Solar Cells. *Energy Environ. Sci.* **2014**, *7*, 3690−3698.

(14) Jeon, N. J.; Noh, J. H.; Kim, Y. C.; Yang, W. S.; Ryu, S.; Seok, S. I. Solvent Engineering for High-Performance Inorganic−Organic Hybrid Perovskite Solar Cells. *Nat. Mater.* **2014**, *13*, 897−903.

(15) Frost, J. M.; Butler, K. T.; Walsh, A. Molecular Ferroelectric Contributions to Anomalous Hysteresis in Hybrid Perovskite Solar Cells. *APL Mater.* **2014**, *2*, 081506.

(16) Wei, J.; Zhao, Y.; Li, H.; Li, G.; Pan, J.; Xu, D.; Zhao, Q.; Yu, D. Hysteresis Analysis Based on the Ferroelectric Effect in Hybrid Perovskite Solar Cells. *J. Phys. Chem. Lett.* **2014**, *5*, 3937−3945.

(17) Chen, H.-W.; Sakai, N.; Ikegami, M.; Miyasaka, T. Emergence of Hysteresis and Transient Ferroelectric Response in Organo-Lead Halide Perovskite Solar Cells. *J. Phys. Chem. Lett.* **2015**, *6*, 164−169.

(18) Shao, Y.; Xiao, Z.; Bi, C.; Yuan, Y.; Huang, J. Origin and Elimination of Photocurrent Hysteresis by Fullerene Passivation in $CH_3NH_3PbI_3$ Planar Heterojunction Solar Cells. *Nat. Commun.* **2014**, *5*, 5784.

(19) Dualeh, A.; Moehl, T.; Tétreault, N.; Teuscher, J.; Gao, P.; Nazeeruddin, M. K.; Grätzel, M. Impedance Spectroscopic Analysis of Lead Iodide Perovskite-Sensitized Solid-State Solar Cells. *ACS Nano* **2014**, *8*, 362−373.

(20) Xiao, Z.; Yuan, Y.; Shao, Y.; Wang, Q.; Dong, Q.; Bi, C.; Sharma, P.; Gruverman, A.; Huang, J. Giant Switchable Photovoltaic Effect in Organometal Trihalide Perovskite Devices. *Nat. Mater.* **2015**, *14*, 193−198.

(21) Kim, H.-S.; Mora-Sero, I.; Gonzalez-Pedro, V.; Fabregat-Santiago, F.; Juarez-Perez, E. J.; Park, N.-G.; Bisquert, J. Mechanism of Carrier Accumulation in Perovskite Thin-Absorber Solar Cells. *Nat. Commun.* **2013**, *4*, 2242.

(22) Kim, H.-S.; Park, N.-G. Parameters Affecting I−V Hysteresis of $CH_3NH_3PbI_3$ Perovskite Solar Cells: Effects of Perovskite Crystal Size and Mesoporous TiO_2 Layer. *J. Phys. Chem. Lett.* **2014**, *5*, 2927−2934.

(23) Fabregat-Santiago, F.; Mora-Seró, I.; Garcia-Belmonte, G.; Bisquert, J. Cyclic Voltammetry Studies of Nanoporous Semiconductors. Capacitive and Reactive Properties of Nanocrystalline TiO_2 Electrodes in Aqueous Electrolyte. *J. Phys. Chem. B* **2003**, *107*, 758−768.

(24) Hass, R.; Garcia-Cañadas, J.; Garcia-Belmonte, G. Electrochemical Impedance Analysis of the Redox Switching Hysteresis of Poly(3,4-ethylenedioxythiophene) Films. *J. Electroanal. Chem.* **2005**, *577*, 99−105.

(25) Bisquert, J. *Nanostructured Energy Devices: Equilibrium Concepts and Kinetics*; CRC Press: Boca Raton, 2014.

(26) Tress, W.; Marinova, N.; Moehl, T.; Zakeeruddin, S. M.; Nazeeruddin, M. K.; Grätzel, M. Understanding the Rate-Dependent $J-V$ Hysteresis, Slow Time Component, and Aging in $CH_3NH_3PbI_3$ Perovskite Solar Cells: the Role of a Compensated Electric Field. *Energy Environ. Sci.* **2015**, *8*, 995−1004.

(27) Onada-Yamamuro, N.; Matsuo, T.; Suga, H. Dielectric Study of $CH_3NH_3PbX_3$ (X = Cl, Br, I). *J. Phys. Chem. Solids* **1992**, *53*, 935−939.

(28) Stoumpos, C. C.; Malliakas, C. D.; Kanatzidis, M. G. Semiconducting Tin and Lead Iodide Perovskites with Organic Cations: Phase Transitions, High Mobilities, and Near-Infrared Photoluminescent Properties. *Inorg. Chem.* **2013**, *52*, 9019−9038.

(29) Frost, J. M.; Butler, K. T.; Brivio, F.; Hendon, C. H.; van Schilfgaarde, M.; Walsh, A. Atomistic Origins of High-Performance in Hybrid Halide Perovskite Solar Cells. *Nano Lett.* **2014**, *14*, 2584−2590.

(30) Poglitsch, A.; Weber, D. Dynamic Disorder in Methylammoniumtrihalogennoplumbates (II) Observed by Millimeter-Wave Spectroscopy. *J. Chem. Phys.* **1987**, *87*, 6373−6378.

(31) Kawamura, Y.; Mashiyama, H.; Hasebe, K. Structural Study on Cubic-Tetragonal Transition of $CH_3NH_3PbI_3$. *J. Phys. Soc. Jpn.* **2002**, *71*, 1694−1697.

DOI: 10.1021/acs.jpclett.5b00480
J. Phys. Chem. Lett. 2015, 6, 1645−1652

(32) Mashiyama, H.; Magome, E.; Kawamura, Y.; Kubota, Y. Displacive Character of the Cubic-Tetragonal Transition in $CH_3NH_3PbX_3$. *J. Korean Phys. Soc.* **2003**, *42*, 1026−1029.
(33) Böttcher, C. J. F.; Belle, O. C. v.; Bordewijk, P.; Rip, A. *Theory of Electric Polarization*; Elsevier Scientific Pub. Co.: Amsterdam/New York, 1973.
(34) Brivio, F.; Walker, A. B.; Walsh, A. Structural and Electronic Properties of Hybrid Perovskites for High-Efficiency Thin-Film Photovoltaics from First-Principles. *APL Mater.* **2013**, *1*, 042113.
(35) Baikie, T.; Fang, Y.; Kadro, J. M.; Schreyer, M.; Wei, F.; Mhaisalkar, S. G.; Graetzel, M.; White, T. J. Synthesis and Crystal Chemistry of the Hybrid Perovskite $(CH_3NH_3)PbI_3$ for Solid-State Sensitised Solar Cell Applications. *J. Mater. Chem. A* **2013**, *1*, 5628.
(36) Guerrero, A.; Juarez-Perez, E. J.; Bisquert, J.; Mora-Sero, I.; Garcia-Belmonte, G. Electrical Field Profile and Doping in Planar Lead Halide Perovskite Solar Cells. *Appl. Phys. Lett.* **2014**, *105*, 133902.
(37) Samiee, M.; Konduri, S.; Ganapathy, B.; Kottokkaran, R.; Abbas, H. A.; Kitahara, A.; Joshi, P.; Zhang, L.; Noack, M.; Dalal, V. Defect Density and Dielectric Constant in Perovskite Solar Cells. *Appl. Phys. Lett.* **2014**, *105*, 153502.
(38) Duan, H.-S.; Zhou, H.; Chen, Q.; Sun, P.; Luo, S.; Song, T.-B.; Bob, B.; Yang, Y. The Identification and Characterization of Defect States in Hybrid Organic−Inorganic Perovskite Photovoltaics. *Phys. Chem. Chem. Phys.* **2015**, *17*, 112−116.
(39) Walter, T.; Herberholz, R.; Müller, C.; Schock, H. W. Determination of Defect Distributions from Admittance Measurements and Application to $Cu(In,Ga)Se_2$ Based Heterojunctions. *J. Appl. Phys.* **1996**, *80*, 4411−4420.
(40) Boix, P. P.; Garcia-Belmonte, G.; Muñecas, U.; Neophytou, M.; Waldauf, C.; Pacios, R. Determination of Gap Defect States in Organic Bulk Heterojunction Solar Cells from Capacitance Measurements. *Appl. Phys. Lett.* **2009**, *95*, 233302.
(41) Hegedus, S. S.; Fagen, E. A. Midgap States in a-Si:H and a-SiGe:H p-i-n Solar Cells and Schottky Junctions by Capacitance Techniques. *J. Appl. Phys.* **1992**, *71*, 5941.
(42) Kim, C.; Tomozawa, M. Electrode Polarization of Glasses. *J. Am. Ceram. Soc.* **1976**, *59*, 127−130.
(43) Serghei, A.; Tress, M.; Sangoro, J. R.; Kremer, F. Electrode Polarization and Charge Transport at Solid Interfaces. *Phys. Rev. B* **2009**, *80*, 184301.
(44) Mitoff, S. P.; Charles, R. J. Electrode Polarization of Ionic Conductors. *J. Appl. Phys.* **1972**, *43*, 927.
(45) Mariappan, C. R.; Heins, T. P.; Roling, B. Electrode Polarization in Glassy Electrolytes: Large Interfacial Capacitance Values and Indication for Pseudocapacitive Charge Storage. *Solid State Ionics* **2010**, *181*, 859−863.
(46) Pitarch, A.; Bisquert, J.; Garcia-Belmonte, G. Mobile Cation Concentration in Ionically Conducting Glasses Calculated by means of Mott−Schottky Capacitance−Voltage Characteristics. *J. Non-Cryst. Solids* **2003**, *324*, 196−200.
(47) Beaumont, J. H.; Jacobs, P. W. M. Polarization in Potassium Chloride Crystals. *J. Phys. Chem. Solids* **1967**, *28*, 657−667.
(48) Wu, X.; Yu, H.; Li, L.; Wang, F.; Xu, H.; Zhao, N. Composition-Dependent Light-Induced Dipole Moment Change in Organometal Halide Perovskites. *J. Phys. Chem. C* **2014**, *119*, 1253−1259.
(49) Gottesman, R.; Haltzi, Eynav; Gouda, L.; Tirosh, S.; Bouhadana, Y.; Zaban, A.; Mosconi, E.; De Angelis, F. Extremely Slow Photoconductivity Response of $CH_3NH_3PbI_3$ Perovskites Suggesting Structural Changes under Working Conditions. *J. Phys. Chem. Lett.* **2014**, *5*, 2662−2669.
(50) Hoke, E. T.; Slotcavage, D. J.; Dohner, E. R.; Bowring, A. R.; Karunadasa, H. I.; McGehee, M. D. Reversible Photo-Induced Trap Formation in Mixed-Halide Hybrid Perovskites for Photovoltaics. *Chem. Sci.* **2015**, *6*, 613.

DOI: 10.1021/acs.jpclett.5b00480
J. Phys. Chem. Lett. 2015, 6, 1645−1652